DOI: 10.31534/engmod.2025.1.ri.06v
Professional paper
Received: 24.10.2023.


# Heat Field Characteristics of Solid Domain of Nozzle Flowmeter with Different Weld Structures

**Yanjuan Zhao**(1), **Jiangbo Tong**(2), **Yuliang Zhang**(3,*)

(1) *College of Information Engineering, Quzhou College of Technology, Quzhou, 324000, Zhejiang, PR CHINA*
*e-mail: zhaoyj05@163.com*

(2) *School of Mechanical Engineering, Hunan University of Technology, Zhuzhou, 412007, Hunan, PR CHINA*
*e-mail: m22080200004@stu.hut.edu.cn*

(3) *College of Mechanical Engineering & Key Laboratory of Air-driven Equipment Technology of Zhejiang Province, Quzhou University, Quzhou, 324000, Zhejiang, PR CHINA*
*e-mail: zhang002@sina.com*

* *Corresponding author*

## SUMMARY

*In this paper, four weld structures with a total of 10 distinct welds were produced and the effect of weld structures on the heat flow field within the solid wall of the nozzle flowmeter is thoroughly investigated by numerical calculations. The results show that, on the path from upstream to downstream, the distance between the weld and nozzle, the width below the weld, the taper angle and the opening have less influence on the heat flow distribution. On the path from the inner to the outer wall, the taper angle and the opening have a greater effect on the peak and the maximum magnitude of the total heat flow, and the peak and the maximum magnitude of the total heat flow for big taper angle and opening welds are much bigger than those under small taper angle and opening welds. The distance between the weld and nozzle, the width below the weld, the taper angle and the opening significantly affect the heat flow distribution of the path section near 0.2 times the length of the monitoring path. However, the heat flow distribution inside the nozzle flowmeter is minimally affected by the distance between the weld and nozzle, the width below the weld, the taper angle and the opening.*

**KEY WORDS:** *nozzle flowmeter; weld structure; heat flow analysis; numerical calculation.*

## 1. INTRODUCTION

In industrial production, serious safety accidents often occur due to weld issues [1,2]. One example is the accident of the large high-pressure steam pipeline "8-11" in Hubei Danyang, in which the weld defects on the accident nozzle expanded under the action of high temperature and high pressure, and local cracks occurred, resulting in steam leakage, creating a hidden

danger of accident [3]. In order to increase the equipment safety, the heat flow field of the nozzle flowmeter under different weld structures needs to be analyzed.

In terms of the impact of the flow of the conveyed medium on the flowmeter's performance, Beck et al. [4] investigated the effect of local turbulence and velocity profiles on the accuracy of an electromagnetic flowmeter and found that the deviation in the accuracy of the flowmeter is disproportionate to the degree of local turbulence. Singh et al. [5] investigated the flow characteristic of a V-cone flowmeter under various Reynolds number and upstream disturbance conditions and discovered that the discharge coefficients are irrelevant to the Reynolds number and that upstream disturbances at farther locations do not affect flow coefficients. Choudhary et al. [6] explored the sound drift effect of ultrasonic flowmeter at different flow rates and different profiles, which is of great significance to improve the signal to noise ratio and reduce the error of flow rate calculation. Jepson et al. [7] found that the instrumentation design has a significant effect on the error due to upstream profile changes and proposed a theoretical model to minimize the error during instrumentation design. Shavrina et al. [8] investigated the effect of gas distribution asymmetry on the multiphase metering accuracy of the Coriolis flowmeter, and discovered that increases in gas volume fraction and decreases in mixing flow rate lead to increases in gas distribution asymmetry and that the gas distribution asymmetry affects the accuracy of the flowmeter. Stone et al. [9] performed an experimental and theoretical study of a viscous flowmeter in a steady and unsteady state. Bobovnik et al. [10] investigated the Coriolis flowmeter under various input velocity circumstances by numerical simulation to assess the effect of flow conditions on performance. Džemić et al. [11] explored the response of a turbine flowmeter to transitional flow regimes and found well response of the turbine flowmeter to accelerated flow and a slower response to decelerated flow.

Regarding structural influences as well as the improvement of measurement accuracy, Ren et al. [12] investigated the response and flow characteristics of the dual-rotor turbine flowmeter through visualization experiments, mathematical calculations and numerical simulations. The results show that the rotor located downstream responds to a smaller flow rate, which increases measurement range; the speed of the rotor located downstream has a compensating effect on the speed calculation, which improves the measurement accuracy. Shavrina [13] investigated the coupled fluid-solid methods for the Coriolis flowmeter and found that both the braces and the entire length of the tube should be considered for the numerical study and that the baseline Reynolds stress model has a higher accuracy than the shear stress turbulence model based on eddy viscosity. Beck et al. [14] explored the effect of short radius on the accuracy of electromagnetic flowmeters and found that laboratory calibration can improve the installation accuracy of electromagnetic flowmeters whether they are installed in a straight pipe or pipe with disturbances upstream. Jin et al. [15] investigated the effects of perforation form, plate thickness, equivalent diameter ratio and hole diameter on the discharge coefficients and pressure loss coefficients of the multi-perforated plate flowmeters. It was found that the perforated plate with a larger center hole diameter is better for liquid hydrogen measurement than the perforated plate with equal hole diameter holes and that the equivalent diameter ratio is the dominant factor affecting the cavitation of liquid hydrogen. Furthermore increasing plate thickness and equivalent diameter ratio improve the performance of the perforated plate. Costa et al. [16] proposed a new model for the Coriolis mass flowmeter for calibration according to the effect from room temperature to low temperatures. Hu et al. [17] simulated the fluid-solid coupling dynamics of a dual U-tube Coriolis flowmeter and found that the unbalanced structure of the dual U-tube leads to zero drift and that the drive current of the voice coil actuator or the pressure loss between the inlet and outlet can determine viscosity. Enz [18] found that any asymmetry in the position of the detector induces a phase shift, leading to incorrect measurements in a Coriolis meter. Anklin et al. [19] explored the effect of sound velocity on flow

measurements of the Coriolis flowmeter and proposed a theory to improve the accuracy. Zhang et al. [20] proposed a theoretical flow correction factor that takes into account the actual velocity distribution to improve the accuracy of ultrasonic propagation in laminar and turbulent flows, and the correction factor matches well with the measured correction factor. Zheng et al. [21] presented a flow numerical integration method based on Gauss quadrature improvement for ultrasonic flowmeters, which significantly improves the measurement performance in disturbed flows. As for the thermal characteristics of the solid domain of flowmeters, only Zhang and Tong et al. [22-24] investigated the heat flow field and thermal effect of different wall temperatures, flow rates and medium with different temperatures on the same nozzle flowmeter. It was found that the heat transfer effect of the nozzle flowmeter decreases with increasing flow rate; when conveying high-temperature media, there is obvious temperature stratification near the inner wall.

From the published literature, the majority of researchers have largely studied flowmeters under various flow circumstances and parameter designs. However, the impact of various weld structures on the heat flow field of the nozzle flowmeter has not been addressed. In this study, the numerical simulation is used to perform calculations on the impact of various weld structures on a nozzle flowmeter's heat flow field. Furthermore, the heat flow field distribution characteristics of the nozzle flowmeter are obtained for different weld structures, which provides guidance and reference for the welding of nozzle flowmeter in high-risk environments and has important significance for improving the safety of the whole transmission pipeline.

## 2. CALCULATION MODEL AND METHOD

### 2.1 FLOWMETER MODEL

The calculation model consists of measuring tubes, weld metal and nozzle, which is exactly the same as that in the literature [23]. Figure 1 shows the flowmeter structures, and Table 1 shows the material attributes of each flowmeter structure.

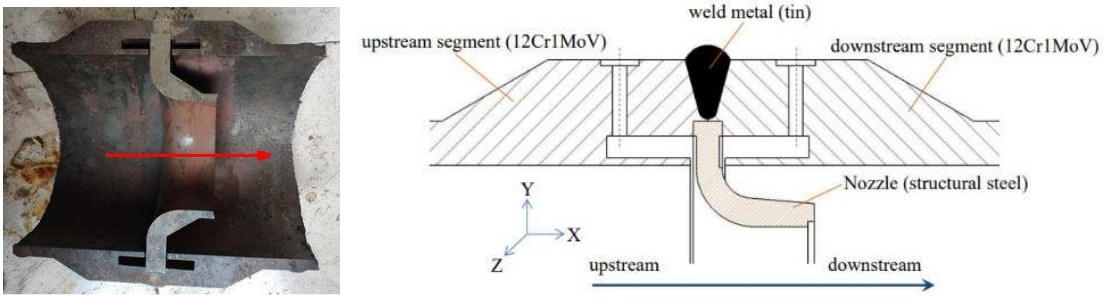


*(a) Real products* *(b) Basic structure*

**Fig. 1** *Overall structure [23]*

**Table 1** *Material properties [25]*

| *Material* | *Density (kg/m³)* | *Isotropic thermal conductivity (W/(m·K))* | *Specific heat (J/(kg·K))* |
|---|---|---|---|
| *12Cr1MoV* | *7860* | *60.5* | *434* |
| *Structural steel* | *7850* | *60.5* | *434* |
| *Tin* | *7304* | *64* | *226.5* |

## 2.2 NUMERICAL SIMULATION METHOD

The modeling was completed using Unigraphics (UG) software and the components are shown in Figure 2(a). The constituent components were divided using unstructured meshes. After the mesh independence test, the final number of elements were determined to be 63875, 1424041, 38623, and 63872 for the front measuring tube, eight slot nozzle, weld metal, and rear measuring tube, respectively, and the total number of elements was 1590411 [23]. Figure 2(b) shows the calculation domain meshes.

The numerical calculation of the structural domain is done using the finite element method based on ANSYS Workbench [26-29]. The heat conduction equation to be solved [26] is:

$$\frac{\partial}{\partial x}(k\frac{\partial T}{\partial x})+\frac{\partial}{\partial y}(k\frac{\partial T}{\partial y})+q=0 \tag{1}$$

where $T$ is the temperature, and $q$ is the heat source equation.

The setting of material properties for each component is shown in Table 1 above. In this paper, the temperature of the conveyed medium is 700℃, so the temperature of wall in contact with the medium is also set to 700℃. The outside walls of the flowmeter are set as the temperature wall, since the environment temperature of the flowmeter is 22℃, the temperature of the outside wall is also set to 22℃. The calculation model in this paper is a nozzle flowmeter after finishing welding, and the contact type between all parts is set to bonded. For the front measuring tube in contact with weld metal, the front measuring tube is set to contact bodies and the weld metal is set to target bodies. For the front measuring tube in contact with the eight-groove nozzle, the front measuring tube is set to contact bodies and the eight-groove nozzle to target bodies. For weld metal in contact with the rear measuring tube, the rear measuring tube is set to contact bodies and the weld metal to target bodies. For the eight-groove nozzle in contact with the rear measuring tube, the eight-groove nozzle is set to contact bodies and the rear measuring tube to target bodies. For weld metal in contact with the eight-groove nozzle, weld metal is set as contact bodies and eight-groove nozzle as target bodies.

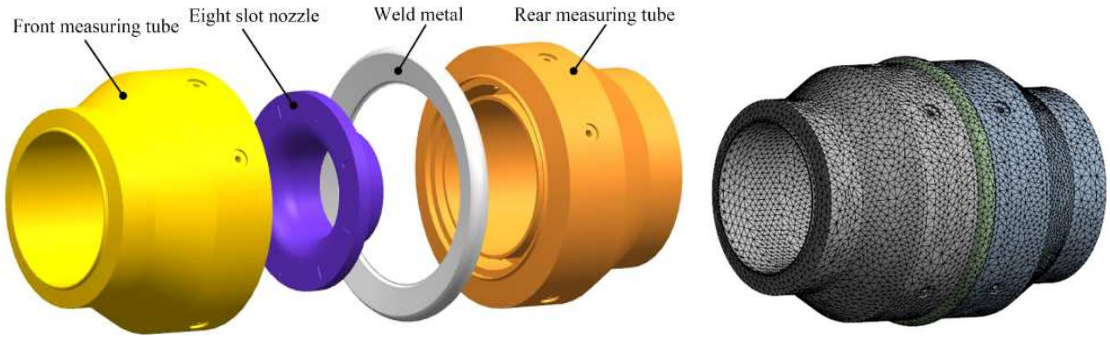


(a) Flowmeter structure (b) Solid field domain mesh

**Fig. 2** *Solid structure and flow field calculation domain schematic*

## 2.3 CALCULATION SCHEME

Four weld structures (I-IV) are designed for the distance between weld and nozzle $L_1$, the width below weld $L_2$, the taper angle $\theta$ and opening $L_3$, with three parameter combinations for each weld structure, as shown in Figure 3. The designed metal welds presented on Figures 4-7 are consistent with those reported in literature [30].

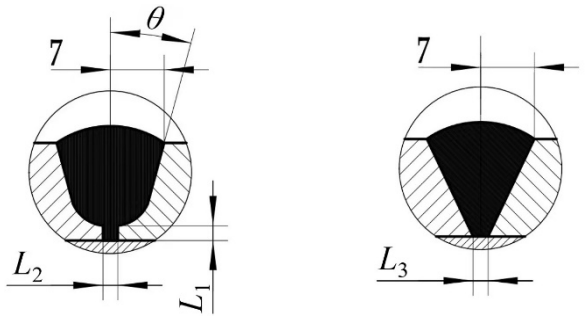


*(a) Type I-III weld structure* *(b) Type IV weld structure*

**Fig. 3** *Schematic of weld structures*

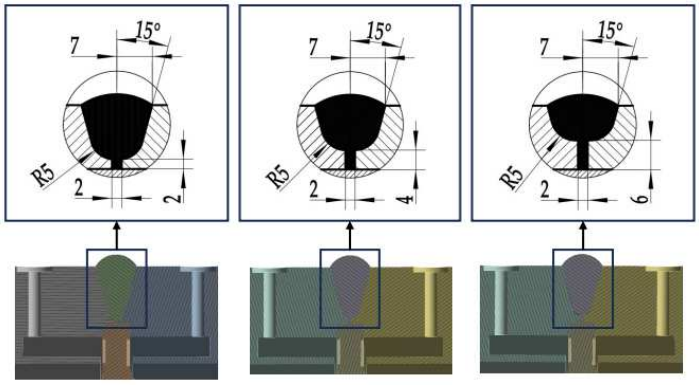


*(a)* *(b)* *(c)*

**Fig. 4** *Cross section of type I weld structure*

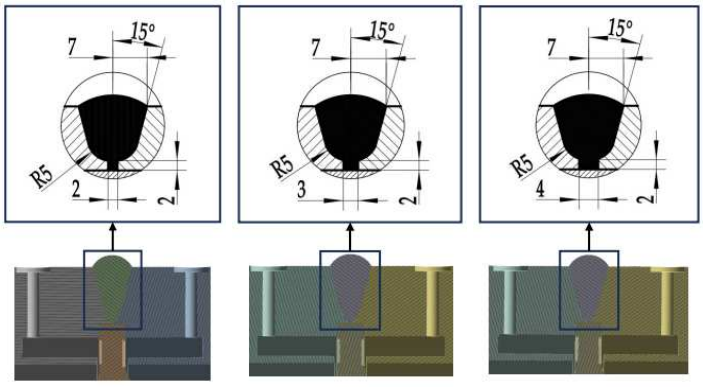


*(a)* *(b)* *(c)*

**Fig. 5** *Cross section of type II weld structure*

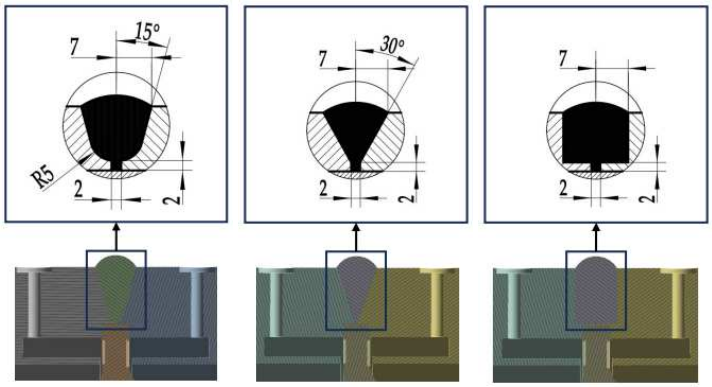


(a) (b) (c)

**Fig. 6** *Cross section of type III weld structure*

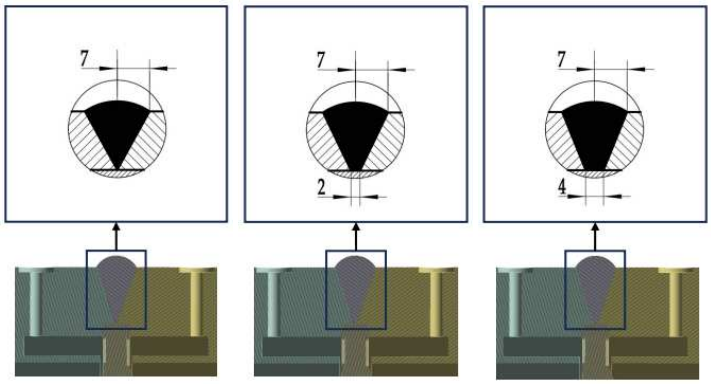


(a) (b) (c)

**Fig. 7** *Cross section of type IV weld structure*

## 3. ANALYSIS OF RESULTS

The monitoring paths of the temperature field are shown in Figure 8 [30]. Monitoring path 1 and path 2 are abbreviated as $P_1$ and $P_2$ in the following text.

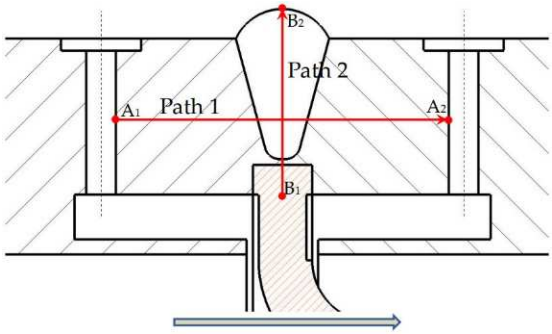


**Fig. 8** *Monitoring path schematic [30]*

## 3.1 HEAT FLOW FIELD OF MONITORING PATHS

### 3.1.1 HEAT FLOW DISTRIBUTION ALONG THE PATH $P_1$

Heat flux [31, 32], sometimes referred to as heat flux density or heat flow density, is the energy flow per unit time per unit area. The heat flow distribution of $P_1$ with different welds is shown in Figure 9. Overall, under each type of weld metal structure, there are four stages of total heat flow change of $P_1$: first, it quickly falls to stable and remains relatively stable; then it quickly falls again to stable and remains relatively stable; then it rises quickly to a steady value and keeps around; and finally, it rises rapidly again. It is also found that the symmetrical distribution of heat flow of $P_1$ is well characterized, and all of them reach the valley between $0.4L$ and $0.6L$. As can be seen for a weld of type I structure, on the path section of $0L$-$0.11539L$, the heat flow decreases rapidly from 2.712W/mm$^2$ to 0.831W/mm$^2$; on the path section of $0.115L$-$0.384L$, the heat flow remains relatively stable; on the path section of $0.385L$-$0.423L$, the heat flow decreases rapidly from 0.833W/mm$^2$ to 0.234W/mm$^2$; on the path section of $0.423L$- $0.577L$, the heat flow remains relatively stable; on the path section of $0.577L$-$0.615L$, the heat flow rapidly increases from 0.234W/mm$^2$ to 0.819W/mm$^2$; on the path section of $0.615L$-$0.885L$, the heat flow remains relatively stable; on the path section of 0.885L-$1.0L$, the heat flow increases rapidly from 0.850W/mm$^2$ to 2.288W/mm$^2$. It is seen that the heat flow has the most variations of plunging, surging, and remaining stable on $P_1$, and the symmetry about the midpoint at $0.5L$ is extremely good.

For the type I structure, the minimum valley value of $P_1$ is 0.226W/mm$^2$, 0.230W/mm$^2$ and 0.234W/mm$^2$ under metal welds of type a, type b and type c, respectively. It is recognized that as $L_1$ increases, the valley value of the total heat flow of $P_1$ increases. In addition, the maximum variation amplitude of $P_1$ is 2.487W/mm$^2$, 2.332W/mm$^2$, and 2.287W/mm$^2$. As the $L_1$ increases, the maximum magnitude of the total heat flow of $P_1$ decreases. It is also found that compared to both ends of $P_1$, the heat flow change curves of type a, b, and c metal welds overlap more in the center section of $P_1$.

For metal welds of types a, b, and c under type II structure, the minimum valley value of $P_1$ is 0.226W/mm$^2$, 0.227W/mm$^2$, and 0.230W/mm$^2$, respectively. As the $L_2$ increases, the valley value of the total heat flow of $P_1$ also increases. Under the same conditions, the maximum magnitude of $P_1$ is 2.487W/mm$^2$, 2.257W/mm$^2$, and 2.272W/mm$^2$, respectively. Similarly to the type I structure, the heat flow curves under the type II structure are extremely coincident in the center section of $P_1$.

For the type III structure, there is a large difference in the variation of heat flow of $P_1$ for type a, b, and c metal welds. In contrast to the other three structures (type I, type II, and type IV), the largest difference in heat flow curves is found in the center section of $P_1$. As $\theta$ increases, the composition of metal materials along $P_1$ is changed significantly: at the center section along $P_1$, the proportion of tin is the least in the type b, and that of type c is the most, wherein that of type a is in the middle. At the same time, due to the different characteristics of the different metals, resulting in different spans of valley region for each type III weld: type b weld has the smallest valley region, type a weld has the middle valley region and type c weld has the largest valley region. However, the change in $\theta$ also has little effect on the total heat flow valley and variation amplitude. Under the type a, b, and c metal welds, the corresponding minimum valley value of $P_1$ is 0.226W/mm$^2$, 0.227W/mm$^2$, and 0.244W/mm$^2$, and the corresponding maximum magnitude of $P_1$ is 2.487W/mm$^2$, 2.305W/mm$^2$ and 2.270W/mm$^2$, respectively.

For type IV structures, the minimum valley value of $P_1$ is 0.227W/mm², 0.228W/mm², and 0.237W/mm² under metal welds of type a, type b and type c. It is clear that as $L_3$ increases, the valley value of the total heat flow of $P_1$ also increases. Furthermore, the maximum magnitude of $P_1$ is 2.630W/mm², 2.534W/mm², and 2.376W/mm², respectively. As can be observed, as $L_3$ increases, the maximum magnitude of the total heat flow of $P_1$ decreases.

Overall, $L_1$, $L_2$, $\theta$ and $L_3$ have little effect on the valley value and the maximum variation amplitude of the total heat flow of $P_1$, but $\theta$ significantly affects the variation of the heat flow situation of $P_1$. Although $L_1$, $L_2$, and $L_3$ change, there is no significant change in the composition of metal materials of $P_1$, and, therefore, the heat flow curves under type I, type II and type IV structures overlap in the center section of $P_1$.

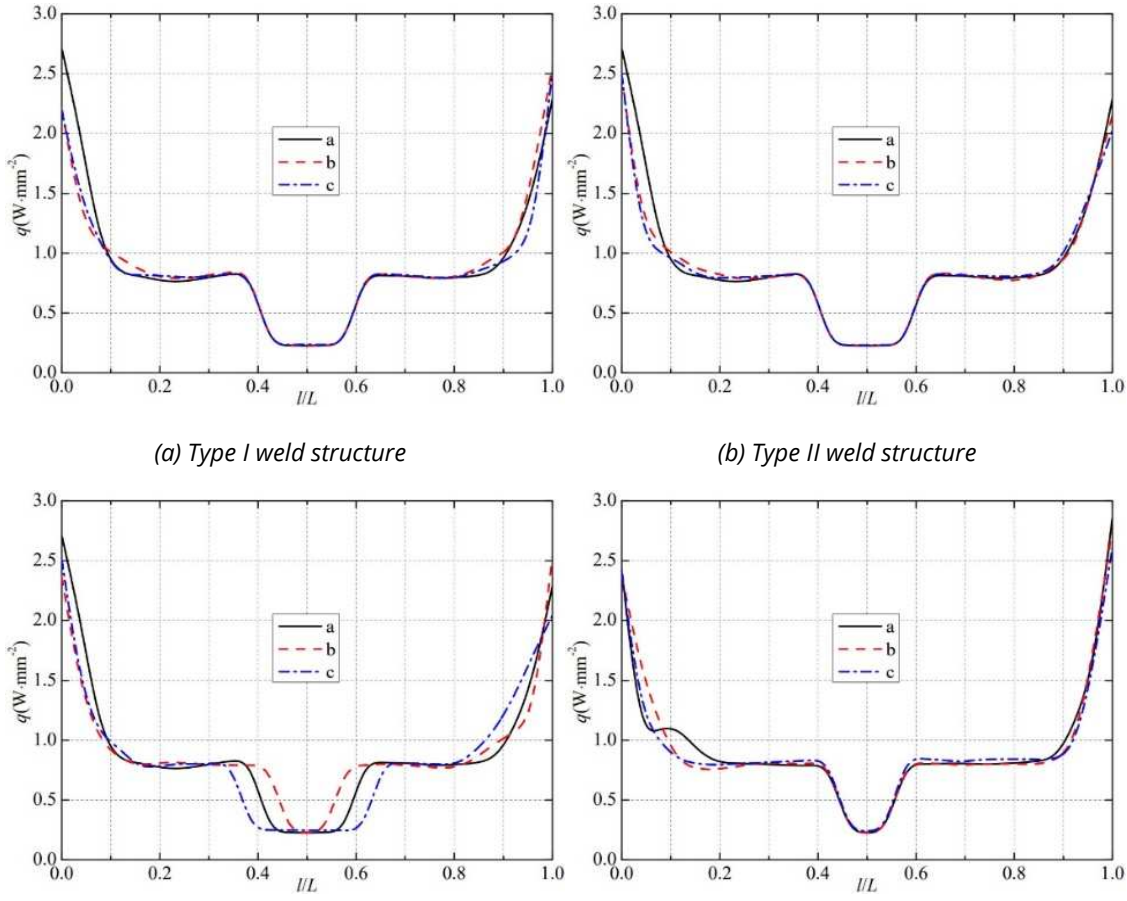


*(a) Type I weld structure* *(b) Type II weld structure*

*(c) Type III weld structure* *(d) Type IV weld structure*

**Fig. 9** *Total heat flow distribution of monitoring path 1*

### 3.1.2 HEAT FLOW DISTRIBUTION ALONG THE PATH $P_2$

The heat flow distribution of $P_2$ with different welds is shown in Figure 10. Under each weld of each structure, the total heat flow of $P_2$ shows an overall trend of increasing and then decreasing. Under type a, b, and c welds of type I structure, the maximum peak value of $P_2$ is 0.227W/mm², 0.237W/mm², and 0.247W/mm², and the maximum magnitude value of $P_2$ is 0.179W/mm², 0.186W/mm² and 0.195W/mm², respectively. It indicates that as $L_1$ increases, the peak and maximum magnitude of the total heat flow of $P_2$ increase. Under type a, b, and c welds of type II

structure, the maximum peak value of $P_2$ is 0.227W/mm², 0.232W/mm², and 0.231W/mm², respectively, and $L_2$ has little effect on the total heat flow peak value of $P_2$. For the three same cases, the maximum magnitude of $P_2$ is 0.179W/mm², 0.183W/mm², and 0.182W/mm², respectively. Altogether, it is clear that compared to the variation in $L_1$, $L_2$ has less effect on the heat flow of $P_2$. The curves overlap more under the type II structure than under the type I structure.

For the type III structure, there is a significant difference in the heat flow curves of $P_2$ of type a, b, and c metal welds. As seen in Figure 9(c), there are small peaks and valleys in the heat flow curves of 0.1$L$-0.3$L$ path of type a and b welds, while the heat flow curves of type c weld shows a monotonically increasing trend. In addition, the largest difference is that the maximum peak of $P_2$ for type c weld is higher than for types a and b. Under type a, b, and c welds of type III structure, the maximum peak value of $P_2$ is 0.226W/mm², 0.227W/mm², and 0.286W/mm², respectively, and the maximum magnitude of $P_2$ is 0.179W/mm², 0.171W/mm² and 0.258W/mm². It indicates that $\theta$ significantly affects the peak and variation amplitude of $P_2$, and the peak value and variation amplitude of the total heat flow are the largest when the $\theta$ is 90°.

Under type a, b, and c welds of type IV structure, the maximum peak value of $P_2$ is 0.228W/mm², 0.230W/mm², and 0.247W/mm², respectively, and the maximum magnitude of $P_2$ is 0.171W/mm², 0.174W/mm² and 0.232W/mm², respectively. It appears that as $L_3$ increases, the peak value and maximum magnitude of the total heat flow of $P_2$ also increase and they are much bigger than those of type a and b for type c weld.

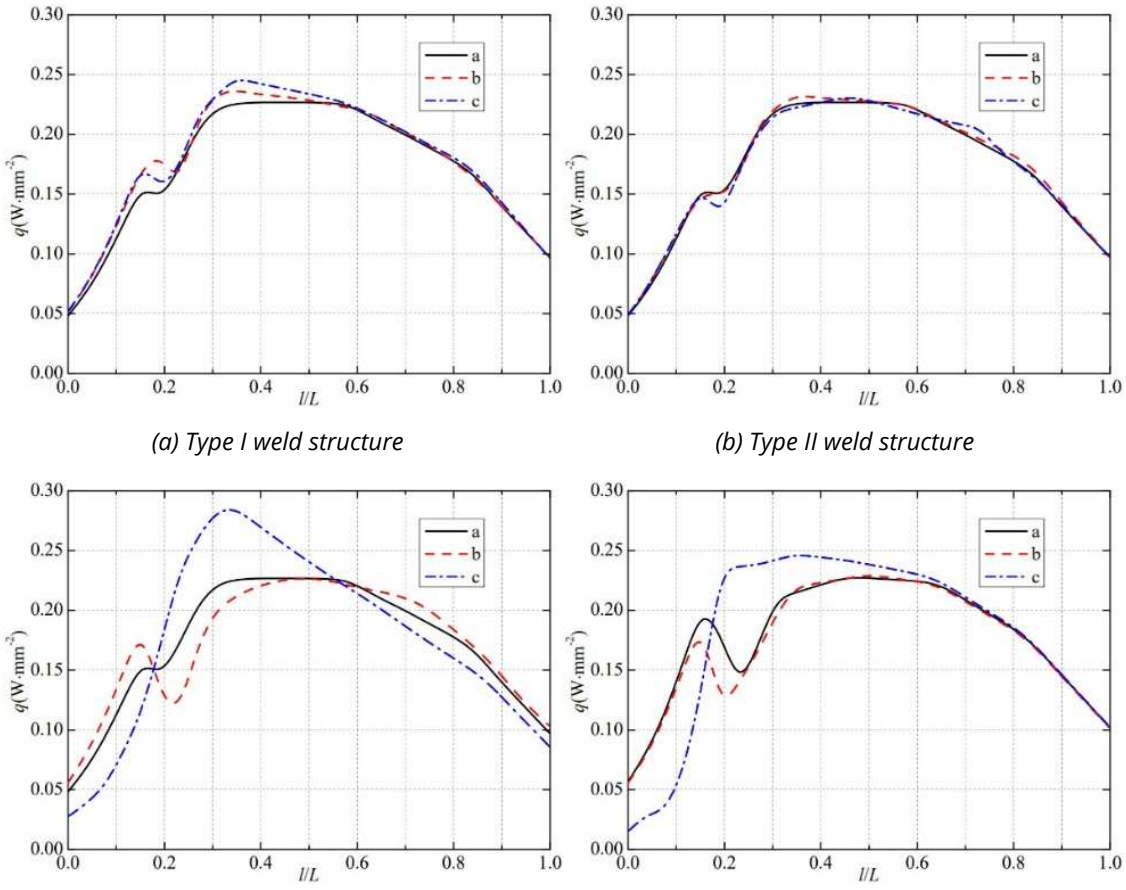


*(a) Type I weld structure* *(b) Type II weld structure*

*(c) Type III weld structure* *(d) Type IV weld structure*

**Fig. 10** *Total heat flow distribution of monitoring path 2*

### 3.1.3 HEAT FLOW DISTRIBUTION ALONG THE PATH $P_1$ IN THE *X* DIRECTION

The heat flow distribution of $P_1$ in the *X* direction with different welds is shown in Figure 11. In the cases of all welds in this study, the heat flow distribution of $P_1$ in the *X* direction shows a decreasing trend and decreases abruptly at the ends of $P_1$, and varies gently between 0.2*L* and 0.8*L*. As can be seen in the type a weld of type I structure, on the path section of 0*L*-0.192*L*, the heat flow decreases abruptly from 2.634W/mm$^2$ to 0.196W/mm$^2$; on the path section of 0.192*L*-0.808*L*, the heat flow varies from 0.196W/mm$^2$ to -0.179W/mm$^2$, on the path section of 0.808*L*-1.0*L*, the heat flow decreases abruptly from -0.179W/mm$^2$ to -2.271W/mm$^2$; and on the path section of 0.808*L*-1.0*L*, the heat flow decreases abruptly from -0.179W/mm$^2$ to -2.271W/mm$^2$. Compared with the variation curves under each weld, the curves have small differences and a high degree of overlap. It can be observed that the variation of the structural parameters has a small effect on the heat flow distribution of $P_1$ in the *X* direction. Also, compared with Figure 8 and Figure 10, on both ends of $P_1$, the absolute value of heat flux on $P_1$ in the *X* direction is slightly smaller than the heat flux on $P_1$, and the changing trend is the same. It indicates that heat energy is conducted mainly in the *X* direction on both ends of $P_1$.

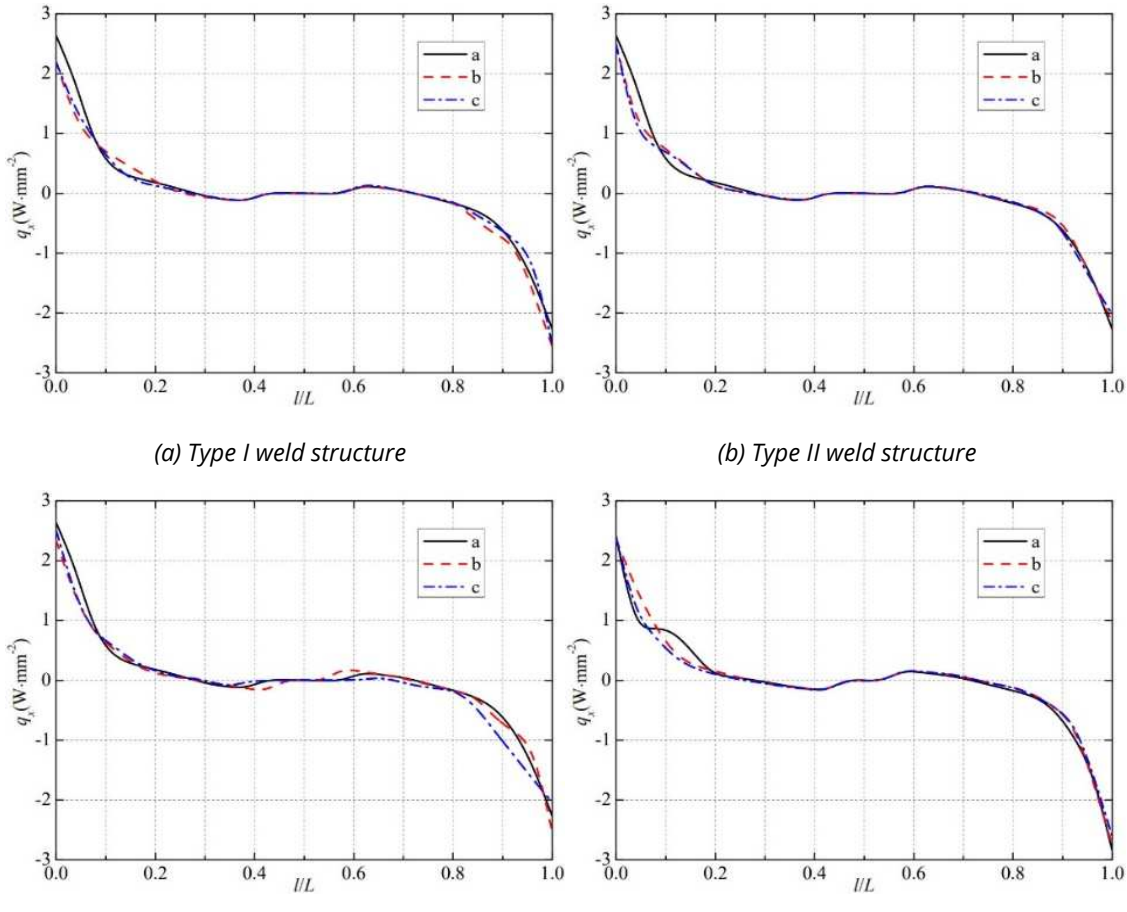


*(a) Type I weld structure*

*(b) Type II weld structure*

*(c) Type III weld structure*

*(d) Type IV weld structure*

**Fig. 11** *Heat flow distribution of monitoring path 1 in the X direction*

#### 3.1.4 HEAT FLOW DISTRIBUTION ALONG THE PATH $P_2$ IN THE *X* DIRECTION

The heat flow distribution of $P_2$ in the *X* direction with different welds is shown in Figure 12. Compared with Figure 9 and Figure 11, the heat flux of $P_2$ is much larger than the absolute value of the heat of $P_2$ in the *X* direction. It shows that the main direction of heat conduction is not the *X* direction on $P_2$. It is also found that under all welds of all types of structures, the values of heat flux in all path sections are extremely small except near $0.2L$; there is a clear change in the curves only near $0.2L$. Different metal characteristics have a significant effect on heat flow. There are two different metal materials, structural steel and tin, on the path section near $0.2L$, and the width of the same metal near $0.2L$ is smaller, and the other metal materials cause more influence, which ultimately results in the peaks and valleys of the *X* direction heat flow on $P_2$ appearing near $0.2L$.

For type a, b, and c metal welds of type I structure, the minimum valley value of the heat flow of $P_2$ in the *X* direction is -0.044W/mm², -0.143W/mm² and -0.094W/mm², respectively, and the maximum magnitude of the heat flow in the *X* direction of $P_2$ is 0.067W/mm², 0.164W/mm² and 0.124W/mm². Clearly, $L_1$ affects both the valley and maximum magnitude of the heat flow of $P_2$ in the *X* direction. For type II, type III, and type IV structures, the heat flow curves have large differences on the path section near $0.2L$, with varying degrees of peaks or valleys. In summary, $L_1$, $L_2$, $\theta$ and $L_3$ all have some effect on the peak, valley, and maximum magnitude of the heat flow of $P_2$ in the *X* direction.

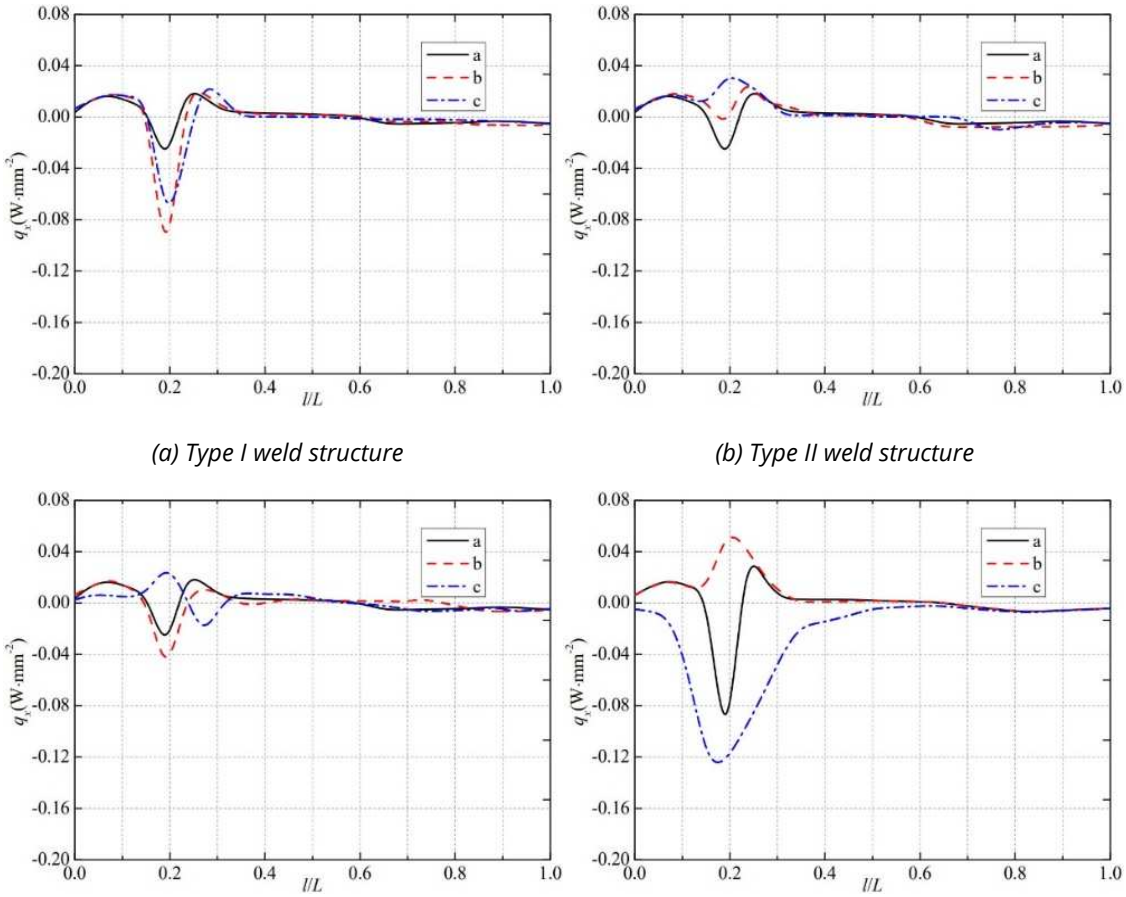


*(a) Type I weld structure*

*(b) Type II weld structure*

*(c) Type III weld structure*

*(d) Type IV weld structure*

**Fig. 12** *Heat flow distribution of monitoring path 2 in the X direction*

#### 3.1.5 HEAT FLOW DISTRIBUTION ALONG THE PATH $P_1$ IN THE *Y* DIRECTION

The heat flow distribution of $P_1$ in the *Y* direction with different welds is shown in Figure 13. With the same characteristics as the heat flow distribution of $P_1$ in the *X* direction, it varies gently from $0.2L$ to $0.8L$, and the heat flux is close to 0. More heat conduction in the *Y* direction is only at the ends of $P_1$. Altogether, the *Y* direction is not the main direction of heat conduction of $P_1$. In addition, comparing the heat flow curves under each weld, it is found that there is a significant difference in the heat flow distribution between the two ends of $P_1$ in the *Y* direction. The variations in $L_1$, $L_2$, $\theta$ and $L_3$ mainly affect the heat flow distribution at both ends of $P_1$ in the *Y* direction.

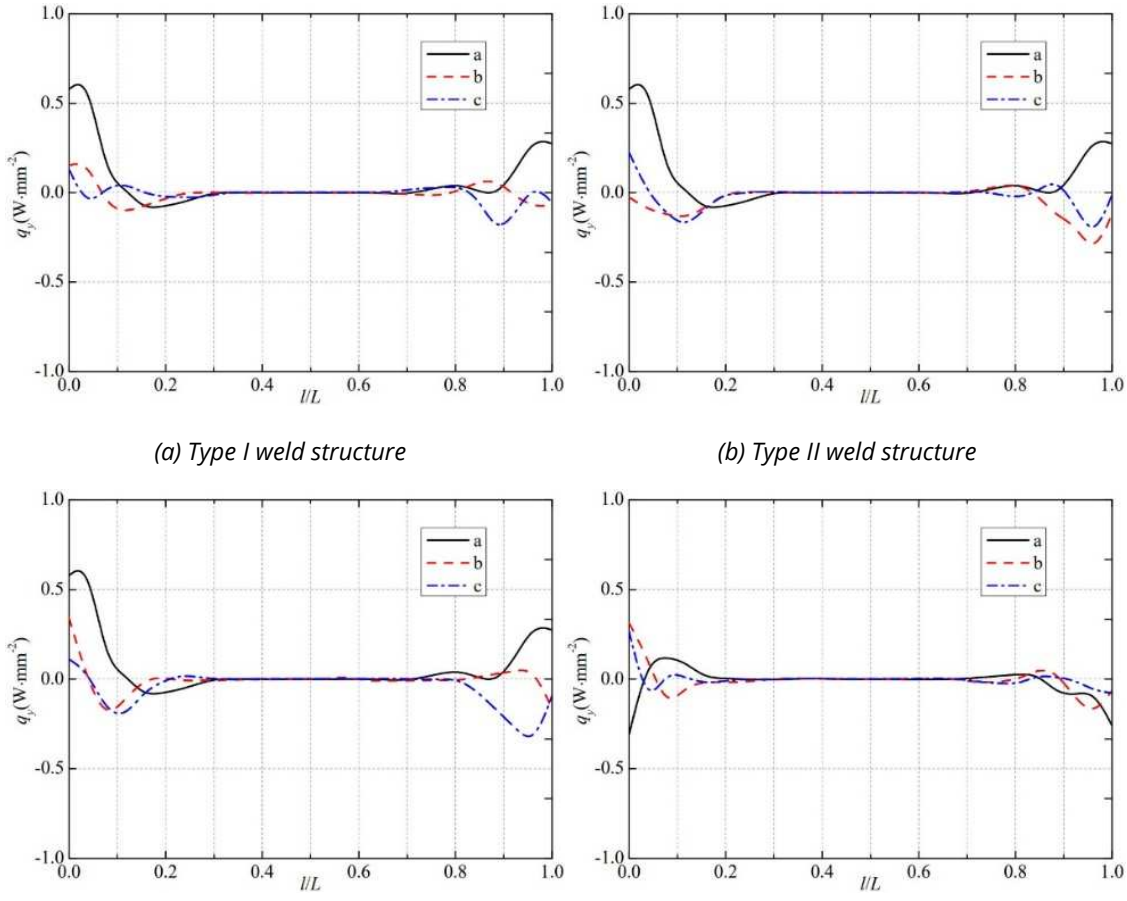


*(a) Type I weld structure* *(b) Type II weld structure*

*(c) Type III weld structure* *(d) Type IV weld structure*

**Fig. 13** *Heat flow distribution of monitoring path 1 in the Y direction*

#### 3.1.6 HEAT FLOW DISTRIBUTION ALONG THE PATH $P_2$ IN THE *Y* DIRECTION

The heat flow distribution of $P_2$ in the *Y* direction with different welds is shown in Figure 14. There is a maximum on the path section near $0.2L$, while all other path sections have minimal heat flow values. For type a, b and c welds of type I structure, the maximum peak value of the heat flow of $P_2$ in the *Y* direction is 0.025W/mm$^2$, 0.010W/mm$^2$ and 0.008W/mm$^2$; for type a, b and c welds of type II structure, the maximum peak value of the heat flow of $P_2$ in the *Y* direction is 0.025W/mm$^2$, 0.015W/mm$^2$ and 0.003W/mm$^2$; for type a, b and c welds of type III structure, the maximum peak value of the heat flow of $P_2$ in the *Y* direction is 0.025W/mm$^2$, 0.015W/mm$^2$

and 0.003W/mm$^2$. It shows that the peak of heat flow of $P_2$ in the $Y$ direction decreases as $L_1$, $L_2$, and $\theta$ increase. For type a, b and c welds of type IV structures, the maximum peak value of the heat flow field of $P_2$ in the $Y$ direction is 0.101W/mm$^2$, 0.007W/mm$^2$ and 0.011W/mm$^2$. The maximum peak value of type a weld of type IV structure is much larger than that of other welds, and $L_3$ significantly affects the heat flow peak of $P_2$ in the $Y$ direction. It is clear that the lower half of the type a weld of type IV structure is "▽" type, the width of the tin is narrower, the influence of the nearby metal is greater and leads to the maximum peak of heat flow of $P_2$ in the $Y$ direction under this weld.

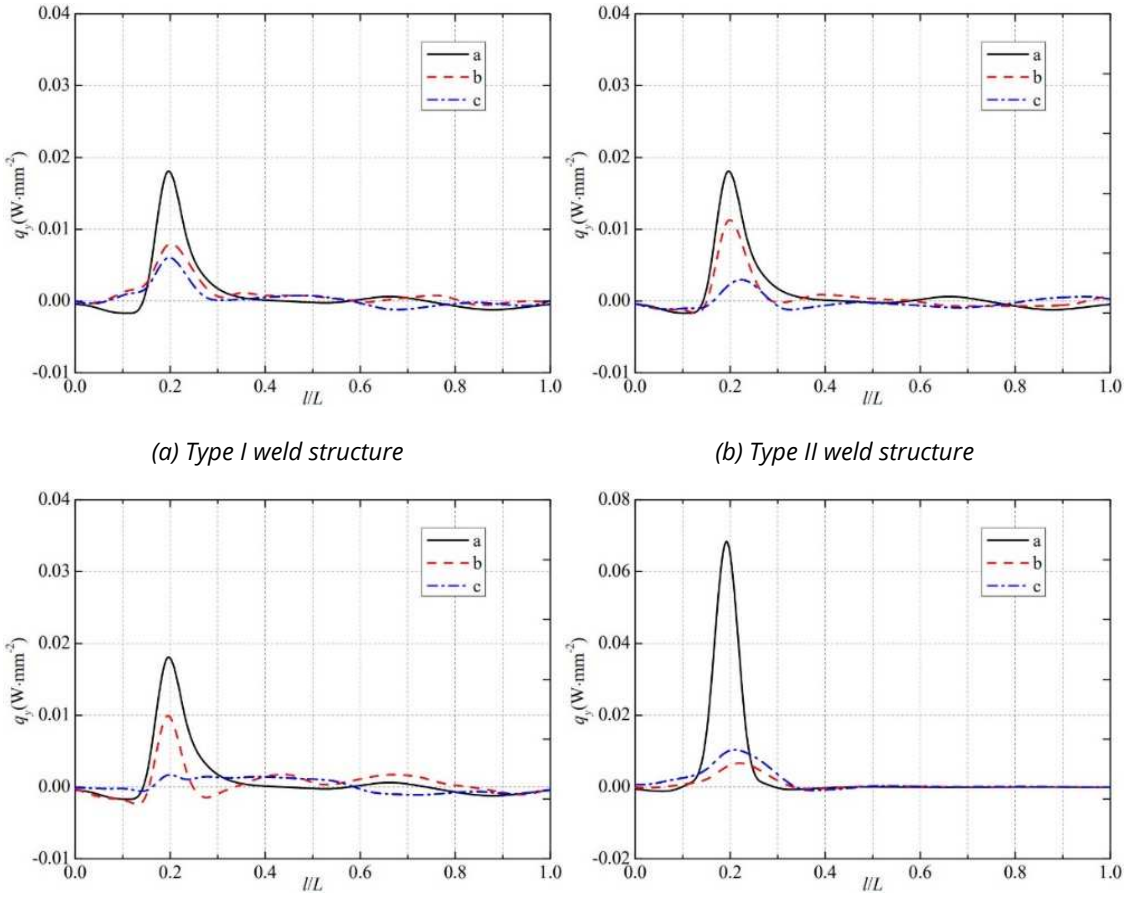


*(a) Type I weld structure* *(b) Type II weld structure*

*(c) Type III weld structure* *(d) Type IV weld structure*

**Fig. 14** *Heat flow distribution of monitoring path 2 in the Y direction*

#### 3.1.7 HEAT FLOW DISTRIBUTION ALONG THE PATH $P_1$ IN THE $Z$ DIRECTION

The heat flow distribution of $P_1$ in the $Z$ direction with different welds is shown in Figure 15. It is found that on the path section of 0.2$L$-0.8$L$, the heat flow of $P_1$ in the $Z$ direction has the same trend as the heat flow of $P_1$ and the values are close to each other. The type a weld of type I structure can be observed as an example. On the path section of 0.192$L$-0.385$L$, the total heat flow changes smoothly from 0.778W/mm$^2$ to 0.833W/mm$^2$, and the heat flow in the $Z$ direction changes smoothly from 0.748W/mm$^2$ to 0.823W/mm$^2$. On the path section of 0.385$L$-0.423$L$, the total heat flow decreases rapidly from 0.833W/mm$^2$ to 0.234W/mm$^2$, and the heat flow in the $Z$ direction decreases rapidly from 0.823W/mm$^2$ to 0.234W/mm$^2$. On the path section of 0.423$L$-0.577$L$, the total heat flow varies smoothly from 0.233W/mm$^2$ to 0.234W/mm$^2$, and the

heat flow in the $Z$ direction varies smoothly from 0.233W/mm$^2$ to 0.234W/mm$^2$. On the path section of 0.577$L$-0.615$L$, the total heat flow increased rapidly from 0.234W W/mm$^2$ to 0.819W/mm$^2$, and the heat flow in the $Z$ direction increased rapidly from 0.234W/mm$^2$ to 0.808W/mm$^2$. On the path section of 0.615$L$-0.808$L$, the total heat flow varies smoothly from 0.819W/mm$^2$ to 0.798W/mm$^2$, and the heat flow in the $Z$ direction varies smoothly from 0.808W/mm$^2$ to 0.776W/mm$^2$. Clearly, the total heat flow on $P_1$ has exactly the same trend as that in the $Z$ direction, and the total heat flow is slightly larger than that in the $Z$ direction. In other words, for the 0.2$L$-0.8$L$ path section of $P_1$, the main direction of heat conduction is the $Z$ direction.

It is found from Figure 15 that the difference in the heat flow curves of $P_1$ in the $Z$ direction is small for type I, type II and type IV weld structures. Compared with the heat flow curves in other three weld structures, it is found that the difference of the heat flow curves at type III structure is the largest in the middle section of the path, especially the valley region spans differently. It indicates that only the change in $\theta$ has a greater effect on the heat flow of $P_1$ in the $Z$ direction.

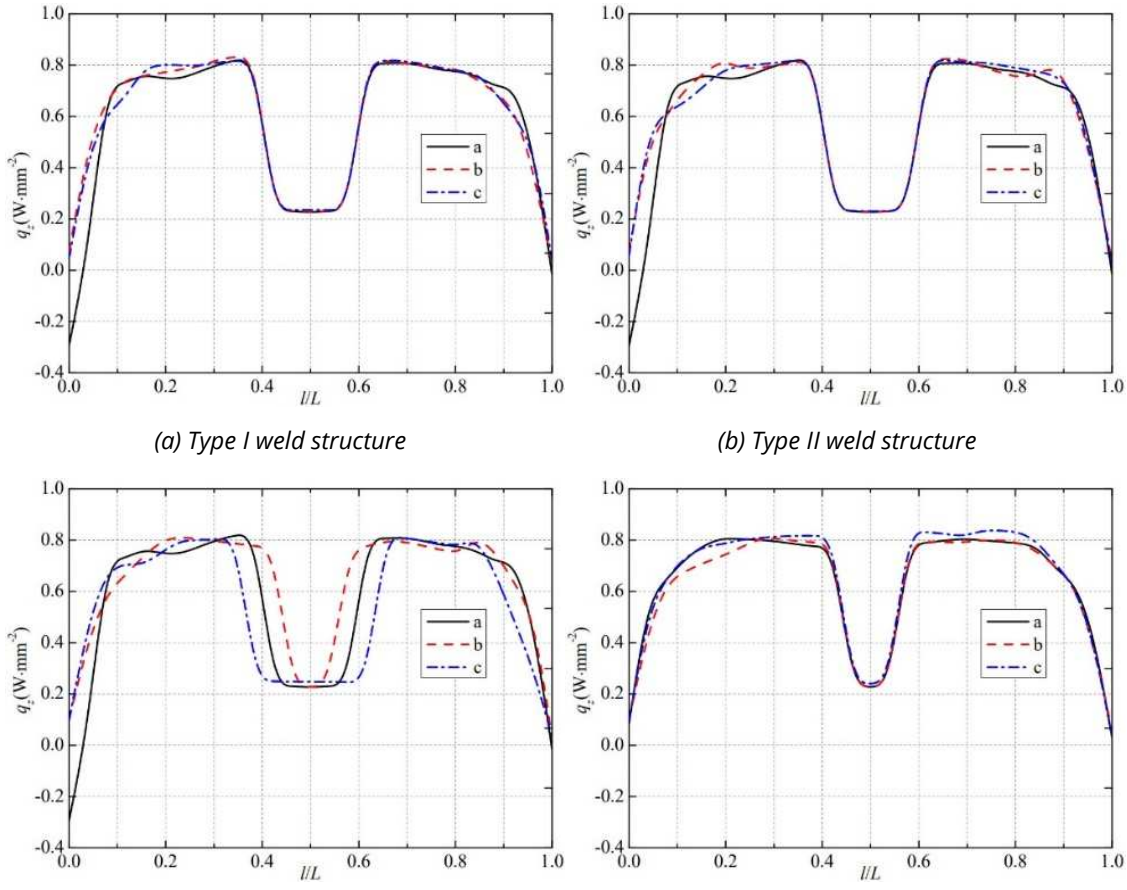


*(a) Type I weld structure* *(b) Type II weld structure*

*(c) Type III weld structure* *(d) Type IV weld structure*

**Fig. 15** *Heat flow distribution of monitoring path 1 in the Z direction*

#### 3.1.8 HEAT FLOW DISTRIBUTION ALONG THE PATH $P_2$ IN THE $Z$ DIRECTION

The heat flow distribution of $P_2$ in the $Z$ direction with different welds is shown in Figure 16. By comparing Figure 16 and Figure 10, it is found that the heat flow trend of $P_2$ in the $Z$ direction under the same weld is close to the total heat flow trend of $P_2$, and the value of heat flow in the

$Z$ direction is slightly smaller than the total heat flow. It is easy to see that the $Z$ direction is the main conduction direction of heat flow on $P_2$.

For type a, b and c nozzle flowmeters of type I structure with inner wall temperature of 700°C, the maximum peak value of the heat flow of $P_2$ in the $Z$ direction is 0.227W/mm$^2$, 0.237W/mm$^2$ and 0.247W/mm$^2$. Obviously, as $L_1$ increases, the peak of heat flow of $P_2$ in the $Z$ direction increases. For type II welds, the maximum peak value of heat flow of $P_2$ in the $Z$ direction is 0.227W/mm$^2$, 0.232W/mm$^2$ and 0.231W/mm$^2$ for type a, b and c, respectively. To sum up, $L_1$ and $L_2$ do not significantly influence the heat flow of $P_2$ in the $Z$ direction: the overlap of the heat flow curves of $P_2$ in the $Z$ direction is high for both type I and type II.

For type III welds, the maximum peak value of heat flow of $P_2$ in the $Z$ direction is 0.227W/mm$^2$, 0.227W/mm$^2$ and 0.286W/mm$^2$ for type a, b and c, respectively. The maximum peak of type c weld is much higher than that of types a and b welds. For the type IV welds, the maximum peak value of heat flow of $P_2$ in the $Z$ direction is 0.228 W/mm$^2$, 0.230 W/mm$^2$, and 0.246 W/mm$^2$, respectively. The maximum peak of type c weld of type IV structure is also much larger than that of types a and b. In addition, the heat flow change curves of $P_2$ in the $Z$ direction for type c welds of type III and type IV structures are more different from those of types a and b. Taken together, $\theta$ and $L_3$ effects on the heat flow of $P_2$ in the $Z$ direction are more significant than those of $L_1$ and $L_2$.

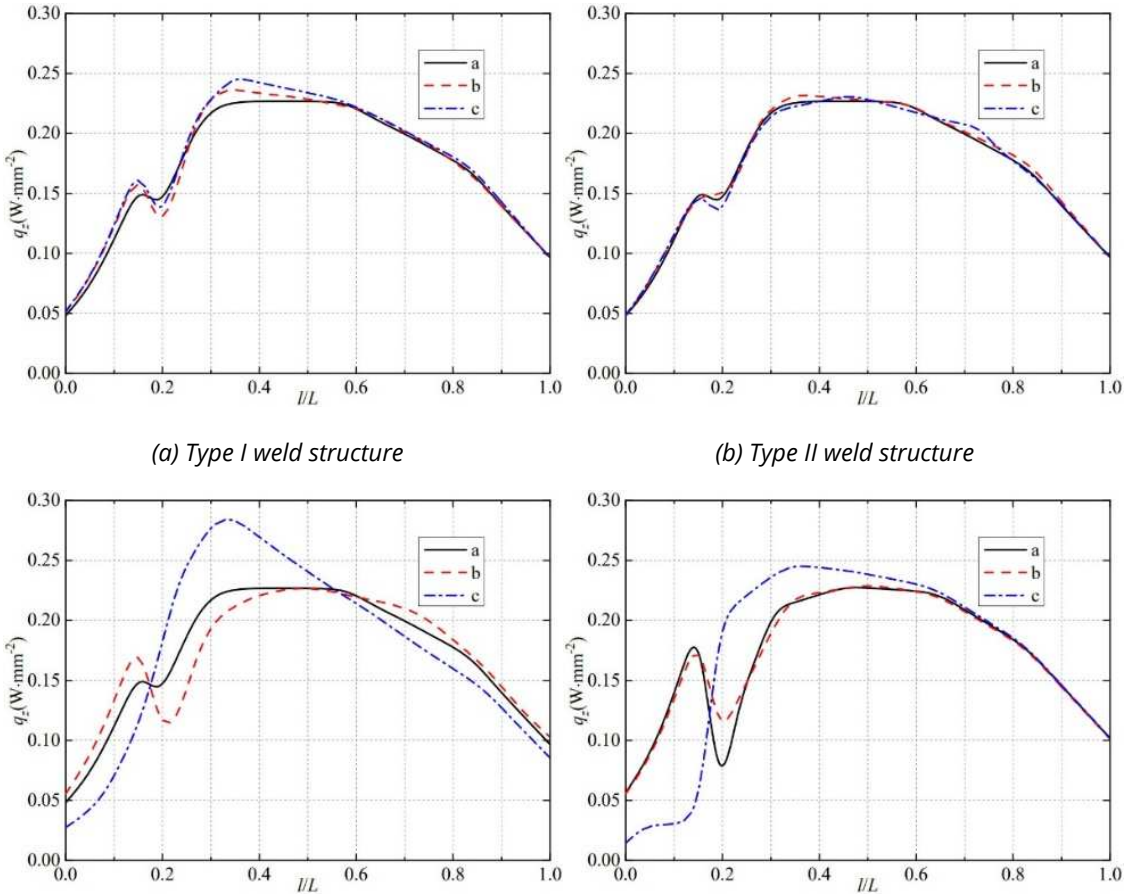


*(a) Type I weld structure*

*(b) Type II weld structure*

*(c) Type III weld structure*

*(d) Type IV weld structure*

**Fig. 16** *Heat flow distribution of monitoring path 2 in the Z direction*

### 3.2 HEAT FLOW FIELD OF SOLID DOMAIN

The total heat flow field of the flowmeter for type I weld is shown in Figure 17. It is clear that the heat flow inside the nozzle flowmeter gradually expands towards the inlet and outlet. Furthermore, the upstream pressure port, downstream pressure port, and inlet and outlet of the type I nozzle flowmeter have a large heat flow area. The maximum value of heat flow occurs at the outlet of all type I nozzle flowmeters with the value of 10W/mm$^2$. The type a, b and c metal welds of the type I structure all exhibit naturally higher heat flow at the inlet, and outlet with the pressure ports. It is evident that $L_1$ has less effect on the internal heat flow.

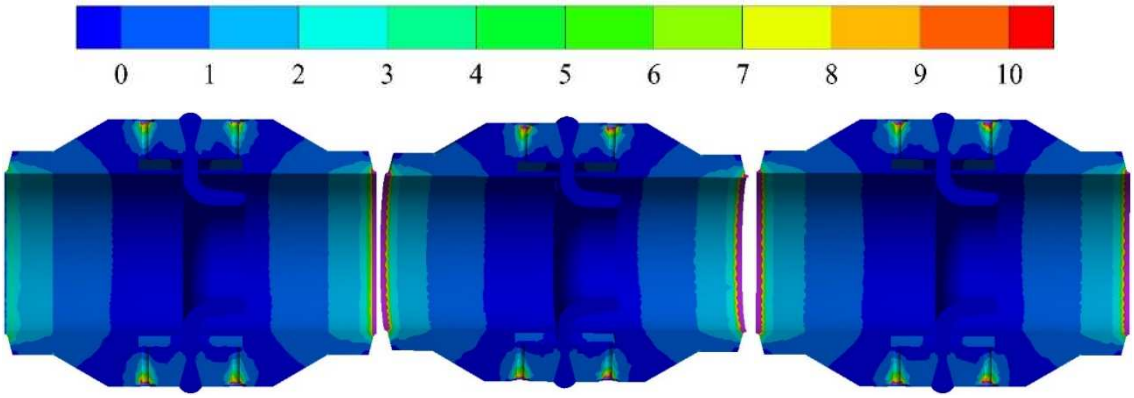


*(a) Type a weld* *(b) Type b weld* *(c) Type c weld*

**Fig. 17** *Total heat flow field in cross section of type I flowmeter (W/mm$^2$)*

The total heat flow field of the flowmeter for type II welds is shown in Figure 18. Same as the flowmeter for type I welds, the heat flow gradually expands to the inlet and outlet, and larger heat flow regions appear in all the same areas. The maximum value of heat flow occurs at the outlet of all type II nozzle flowmeters with the value of 10W/mm$^2$. The type a, b and c metal welds of the type II structure all exhibit naturally higher heat flow at the inlet and outlet with the pressure ports. Clearly, $L_2$ has less effect on the internal heat flow distribution.

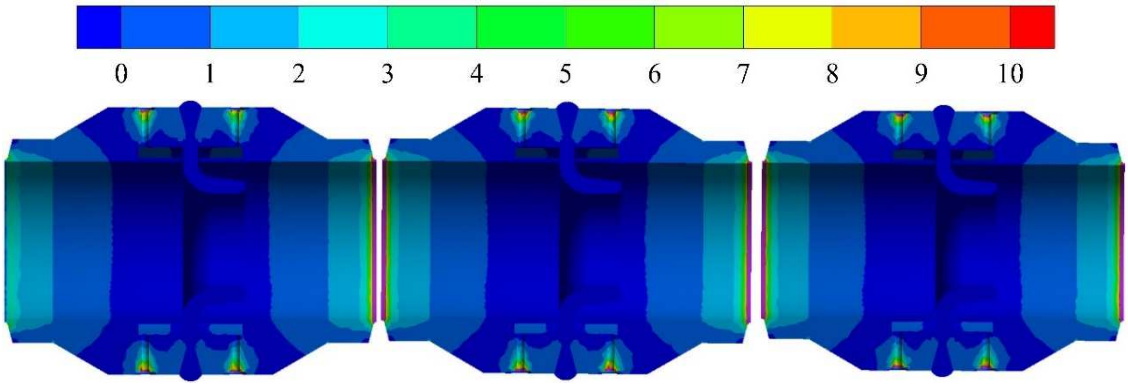


*(a) Type a weld* *(b) Type b weld* *(c) Type c weld*

**Fig. 18** *Total heat flow field in cross section of type II flowmeter (W/mm$^2$)*

The total heat flow field of the flowmeter for type III weld is shown in Figure 19. Similarly to the previous two structures, the flowmeter heat flow of Structure III welds also extends to both sides, and larger heat flow regions also appear at the upstream and downstream pressure ports and at the inlet and outlet of the type III nozzle flowmeters. The maximum value of heat flow occurs at the outlet of the nozzle flowmeter of type III structure with the value of 10W/mm$^2$. The type a, b and c metal welds of type III structure all show naturally higher heat flow at the inlet and outlet with the pressure ports. This shows that $\theta$ has less effect on the internal heat flow distribution.

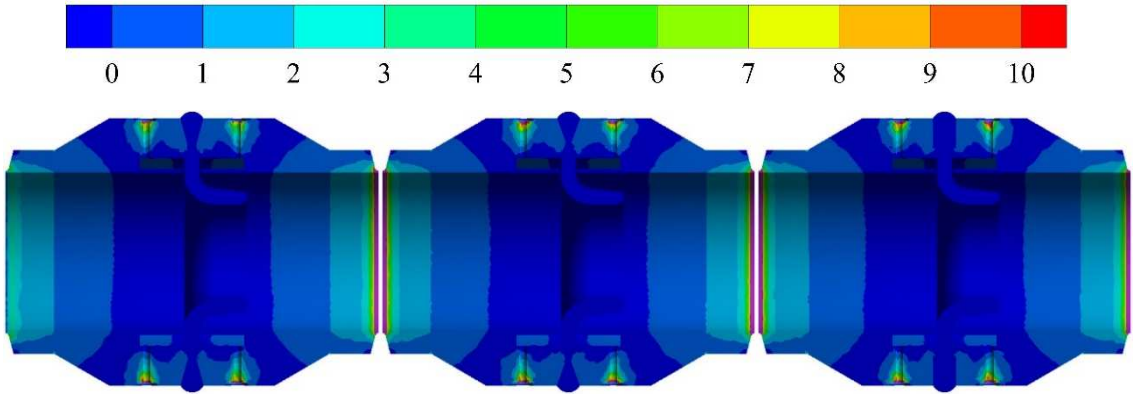


*(a) Type a weld* *(b) Type b weld* *(c) Type c weld*

**Fig. 19** *Total heat flow field in cross section of type III flowmeter (W/mm$^2$)*

The total heat flow field of the flowmeter for type IV weld is shown in Figure 20. As can be seen, the heat flow inside the type IV nozzle flowmeter also gradually expands towards the inlet and outlet. Moreover, there are large heat flow areas at the upstream and downstream pressure ports and the inlet and outlet of the Type IV nozzle flowmeter. The maximum value of heat flow occurs at the inlet and outlet of all type IV nozzle flowmeters with the value of 10W/mm$^2$. Furthermore, type a, b and c welds of type IV structure all exhibit naturally higher heat flow at the inlet and outlet with the pressure ports. It can be seen that $L_3$ has a small effect on the internal heat flow distribution.

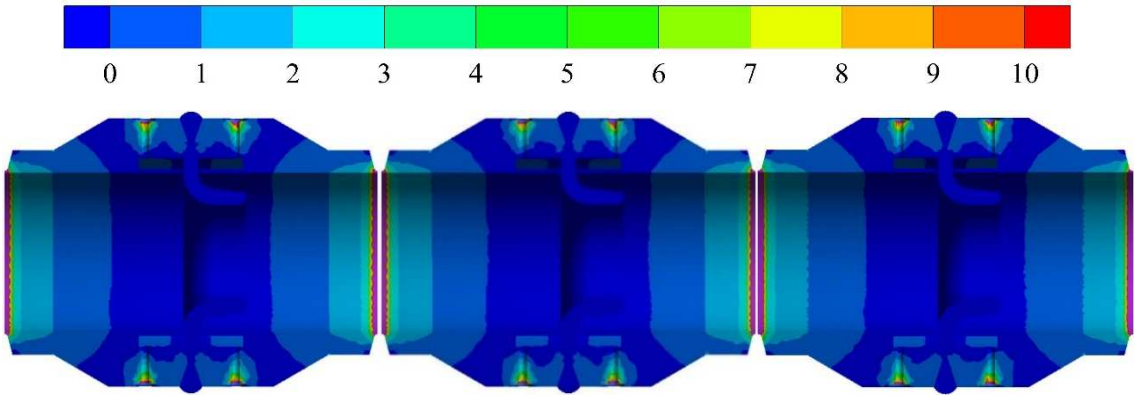


*(a) Type a weld* *(b) Type b weld* *(c) Type c weld*

**Fig. 20** *Total heat flow field in cross section of type IV flowmeter (W/mm$^2$)*

### 3.3 DISCUSSION

The study is basic research, which grasps the heat flow field characteristics under different weld structures, provides a reference for the structural optimization of the weld, and has certain significance for improving the welding safety of nozzle flowmeters and pipeline safety. In this study, initially, only the finite element method was used to predict the thermal field characteristics in the solid domain of the nozzle flowmeter. However, due to the differences in different models, the accuracy of the calculation results is to be verified in future work. In addition, this paper only explores the thermal flow field characteristics when the metal material is tin. The influence of other materials on the thermal flow field characteristics is also to be examined in future work.

## 4. CONCLUSION

Under different welds, on the path from upstream to downstream (i.e., $P_1$), the total heat flow changes mostly show the trend of plummeting, rising and remaining stable, and the symmetrical distribution of heat flow is very clear, all reaching the valley value between $0.4L$ and $0.6L$. The distance between the weld and nozzle $L_1$, the width below weld $L_2$, the taper angle $\theta$ and the taper opening $L_3$ have a small effect on the valley and the maximum variation amplitude of the total heat flow in this path, but there is a significant effect of $\theta$ on the middle part of the path.

On the path from the inner to the outer wall (i.e., $P_2$), the total heat flow changes in the overall trend, first increasing and then decreasing. Compared to $L_1$ and $L_2$, $\theta$ and $L_3$ significantly affect the peak and maximum variation amplitude of the total heat flow on this path: the peak value and the maximum amplitude of the total heat flow are much larger for type c welds of types III and IV than for types a and b.

The heat energy at both ends of the path is mainly conducted in the $X$ direction along $P_1$, and the heat energy on the $0.2L$-$0.8L$ path section is mainly conducted in the $Z$ direction. The $Z$ direction along $P_2$ is the main conduction direction of heat flow.

At $P_1$, $L_1$ and $L_2$ as well as $\theta$ and $L_3$ have a smaller influence on the heat flow distribution in the $X$, $Y$ and $Z$ directions and a greater influence only on the heat flow field in the $Y$ direction at the two ends of the path. $L_1$ and $L_2$, as well as $\theta$ and $L_3$ significantly affect the heat flow distributions in the $X$ and $Y$ directions of the near $0.2L$ path section at $P_2$.

The heat flow inside the nozzle flowmeter gradually expands toward the inlet and outlet, and larger heat flow regions appear at both the upstream and downstream pressure ports as well as the inlet and outlet. $L_1$ and $L_2$ as well as $\theta$ and $L_3$ have less effect on the heat flow distribution inside the nozzle flow meter.

## 5. ACKNOWLEDGMENT

The research was financially supported by the Science and Technology Project of Quzhou (No.2023K256) and Research Grants Program of Department of Education of Zhejiang Province (No. Y202455709).

## 6. REFERENCES

[1] Feng, Q.S., Li, R., Nie, B.H., Liu, S.C., Zhao, L.Y., Zhang, H., Literature review: Theory and application of in-line inspection technologies for oil and gas pipeline girth weld defection, *Sensors*, Vol. 17, No. 1, article number 50, 2016. https://doi.org/10.3390/s17010050

[2] Wang, T., Yang, H., Feng, Q.S., Zhou, L.J., Wang, F.X., Xiang, X.Q., Current status and prospect of inline inspection technologies for defects in girth weld of oil and gas pipeline, *Oil Gas Storage Transp*, Vol. 34, No. 7, pp. 694-698, 2015.
http://www.cnki.net/kcms/detail/13.1093.TE.20150114.1600.008.html

[3] Deng, H.X., Hubei Danyang City Madian Gangue Power Co., Ltd. "8-11" major high-pressure steam pipeline cracked and exploded accident, *Xiandai Banzu*, Vol. 2018, No. 2, pp. 29, 2018.

[4] Beck, K.J., Barfuss, S.L., Johnson, M.C., Assessing the effects of local turbulence and velocity profiles on electromagnetic flowmeter accuracy, *AWWA Water Science*, Vol. 1, No. 5, article number e1156, 2019. https://doi.org/10.1002/aws2.1156

[5] Singh, S.N., Seshadri, V., Singh, R.K., Gawhade, R., Effect of upstream flow disturbances on the performance characteristics of a V-cone flowmeter, *Flow Measurement and Instrumentation*, Vol. 17, No. 5, pp. 291-297, 2006.
https://doi.org/10.1016/j.flowmeasinst.2006.08.003

[6] Choudhary, K.P., Arumuru, V., Bhumkar, Y.G., Numerical simulation of beam drift effect in ultrasonic flow-meter, *Measurement*, Vol. 146, pp. 705-717, 2019.
https://doi.org/10.1016/j.measurement.2019.06.044

[7] Jepson, P., Bean, P.G., Effect of upstream velocity profiles on turbine flowmeter registration, *Journal of Mechanical Engineering Science*, Vol. 11, No. 5, pp. 503-510, 1969.
https://doi.org/10.1243/JMES_JOUR_1969_011_061_02

[8] Shavrina, E., Zeng, Y., Khoo, B.C., Nguyen, V.T., The investigation of gas distribution asymmetry effect on coriolis flowmeter accuracy at multiphase metering, *Sensors*, Vol. 22, No. 20, article number 7739, 2022. https://doi.org/10.3390/s22207739

[9] Stone, C.R., Wright, S.D., Non-linear and unsteady flow analysis of flow in a viscous flowmeter, *Transactions of the Institute of Measurement and Control*, Vol. 16, No. 3, pp. 128-141, 1994. https://doi.org/10.1177/014233129401600302

[10] Bobovnik, G., Kutin, J., Bajsić, I., The effect of flow conditions on the sensitivity of the Coriolis flowmeter, *Flow Measurement and Instrumentation*, Vol. 15, No. 2, pp. 69-76, 2004. https://doi.org/10.1016/j.flowmeasinst.2003.12.001

[11] Džemić, Z., Širok, B., Bizjan, B., Turbine flowmeter response to transitional flow regimes, *Flow Measurement and Instrumentation*, Vol. 59, pp. 18-22, 2018.
https://doi.org/10.1016/j.flowmeasinst.2017.11.006

[12] Ren, Z.P., Zhou, W.X., Li, D.Y., Response and flow characteristics of a dual-rotor turbine flowmeter, *Flow Measurement and Instrumentation*, Vol. 83, article number 102120, 2022. https://doi.org/10.1016/j.flowmeasinst.2022.102120

[13] Shavrina, E., Nguyen, V.T., Yan, Z., Khoo, B.C., Fluid-solid interaction simulation methodology for coriolis flowmeter operation analysis, *Sensors*, Vol. 21, No. 23, article number 8105, 2021. https://doi.org/10.3390/s21238105

[14] Beck, K.J., Weller, R.P., Barfuss, S.L., Johnson, M.C., The effects of a short-radius elbow on electromagnetic flowmeter accuracy, *Journal-American Water Works Association*, Vol. 110, No. 7, pp. E12-E17, 2018. https://doi.org/10.1002/awwa.1055

[15] Jin, T., Tian, H., Gao, X., Liu, Y.L., Wang, J., Chen, H., Lan, Y.Q., Simulation and performance analysis of the perforated plate flowmeter for liquid hydrogen, *International Journal of Hydrogen Energy*, Vol. 42, No. 6, pp. 3890-3898, 2017.
https://doi.org/10.1016/j.ijhydene.2016.09.072

[16] Costa, F.O., Pope, J.G., Gillis, K.A., Modeling temperature effects on a Coriolis mass flowmeter, *Flow Measurement and Instrumentation*, Vol. 76, article number 101811, 2020.

https://doi.org/10.1016/j.flowmeasinst.2020.101811

[17] Hu, Y.C., Chen, Z.Y., Chang, P.Z., Fluid–structure coupling effects in a dual U-tube Coriolis mass flow meter, *Sensors*, Vol. 21, No. 3, article number 982, 2021. https://doi.org/10.3390/s21030982

[18] Enz, S., Effect of asymmetric actuator and detector position on Coriolis flowmeter and measured phase shift, *Flow Measurement and Instrumentation*, Vol. 21, No. 4, pp. 497-503, 2010. https://doi.org/10.1016/j.flowmeasinst.2010.07.003

[19] Anklin, M., Eckert, G., Sorokin, S., Wenger, A., Effect of finite medium speed of sound on Coriolis mass flowmeter, Proceedings of the 10th International Flow Measurement Conference, 2000.

[20] Zhang, H., Guo, C.W., Lin, J., Effects of velocity profiles on measuring accuracy of transit-time ultrasonic flowmeter, *Applied Sciences*, Vol. 9, No. 8, article number 1648, 2019. https://doi.org/10.3390/app9081648

[21] Zheng, D.D., Zhao, D., Mei, J.Q., Improved numerical integration method for flowrate of ultrasonic flowmeter based on Gauss quadrature for non-ideal flow fields, *Flow Measurement and Instrumentation*, Vol. 41, pp. 28-35, 2015. https://doi.org/10.1016/j.flowmeasinst.2014.10.005

[22] Zhang, Y.L., Tong, L.H., Xiao, J.J., Zhang, K.Y., Influence of wall temperature on thermal effect of nozzle flowmeter, *Frontiers in Heat and Mass Transfer (FHMT)*, Vol. 18, article number 38, 2022. https://doi.org/10.5098/hmt.18.38

[23] Tong, L.H., Zheng, S.L., Zhang, Y.L., Zhao, Y.J., Zhang, K.Y., Li, J.F., Study on thermal effect of nozzle flowmeter based on fluid-solid coupling method, *Shock and Vibration*, Vol. 2021, pp. 1-11, 2021. https://doi.org/10.1155/2021/7448439

[24] Tong, L.H., Zhang, Y.L., Yu, T.H., Luo, B.Y., Li, J.F., Heat flow distribution characteristics of solid wall of nozzle flowmeter, *Frontiers in Heat and Mass Transfer (FHMT)*, Vol. 20, article number 10, 2023. https://doi.org/10.5098/hmt.20.10

[25] Huang, Z.X., *ANSYS Workbench handbook 16.0*, People Post Press, 2016.

[26] Abidin, M.N.Z., Misro, M.Y., Numerical simulation of heat transfer using finite element method, *Journal of Advanced Research in Fluid Mechanics and Thermal Sciences*, Vol. 92, No. 2, pp. 104-115, 2022. https://doi.org/10.37934/arfmts.92.2.104115

[27] Alagusundaram, K., Jayas, D.S., White, N.D.G., Muir, W.E., Three-dimensional, finite element, heat transfer model of temperature distribution in grain storage bins, *Transactions of the ASAE*, Vol. 33, No. 2, pp. 577-584, 1990. https://doi.org/10.13031/2013.31369

[28] Sedighi, M.R., Dardashti, B.N., Heat transfer modeling in multi-layer cookware using finite element method, *International Journal of Science and Engineering Investigations*, 2012, Vol. 1, No. 1, pp. 190-196, 2012.

[29] Wilson, E.L., Nickell, R.E., Application of the finite element method to heat conduction analysis, *Nuclear Engineering and Design*, Vol. 4, No. 3, pp. 276-286, 1966. https://doi.org/10.1016/0029-5493(66)90051-3

[30] Zhang, Y.L., Tong, J.B., Zhu, Z.C., Effect of weld shape on temperature field of nozzle flowmeter, *Processes*, Vol. 11, No. 7, pp.1-12, 2023. https://doi.org/10.3390/pr11072164

[31] Fuchs, M., Heat Flux, *Methods of Soil Analysis: Part 1 Physical and Mineralogical Methods*, Vol. 5, pp. 957-968, 1986. https://doi.org/10.2136/sssabookser5.1.2ed.c40

[32] Philip, J.R., The theory of heat flux meters, *Journal of Geophysical Research*, Vol. 66, No. 2, pp. 571-579, 1961. https://doi.org/10.1029/JZ066i002p00571